First-principles simulation of electron mean-free-path spectra and thermoelectric properties in silicon

2015 EPL 109 57006

(http://iopscience.iop.org/0295-5075/109/5/57006)

A Letters Journal Exploring the Frontiers of Physics

March 2015

EPL, **109** (2015) 57006
doi: 10.1209/0295-5075/109/57006

www.epljournal.org

First-principles simulation of electron mean-free-path spectra and thermoelectric properties in silicon

Bo Qiu[1], Zhiting Tian[1], Ajit Vallabhaneni[2], Bolin Liao[1], Jonathan M. Mendoza[1], Oscar D. Restrepo[3], Xiulin Ruan[2] and Gang Chen[1(a)]

[1] *Mechanical Engineering, Massachusetts Institute of Technology - Cambridge, MA, USA*
[2] *Mechanical Engineering, Purdue University - West Lafayette, IN, USA*
[3] *Materials Science and Engineering, Ohio State University - Columbus, OH, USA*

received 26 September 2014; accepted in final form 23 February 2015
published online 12 March 2015

PACS 72.20.Pa – Thermoelectric and thermomagnetic effects
PACS 65.80.-g – Thermal properties of small particles, nanocrystals, nanotubes, and other related systems
PACS 72.10.-d – Theory of electronic transport; scattering mechanisms

Abstract – The mean free paths (MFPs) of energy carriers are of critical importance to the nanoengineering of better thermoelectric materials. Despite significant progress in the first-principles–based understanding of the spectral distribution of phonon MFPs in recent years, the spectral distribution of electron MFPs remains unclear. In this work, we compute the energy-dependent electron scatterings and MFPs in silicon from first principles. The electrical conductivity accumulation with respect to electron MFPs is compared to that of the phonon thermal conductivity accumulation to illustrate the quantitative impact of nanostructuring on electron and phonon transport. By combining all electron and phonon transport properties from first principles, we predict the thermoelectric properties of the bulk and nanostructured silicon, and find that silicon with 20 nm nanograins can result in a higher than five times enhancement in their thermoelectric figure of merit as the grain boundaries scatter phonons more significantly than that of electrons due to their disparate MFP distributions.

Nanostructuring has proven to be an effective strategy to improve the figure of merit of thermoelectric materials [1–11]. The figure of merit is proportional to the electrical conductivity (σ), the square of the Seebeck coefficient (S) and inversely proportional to the thermal conductivity consisting of both phonon (k_p) and electron (k_e) contributions. The most effective nanostructuring approach so far has been reducing the phonon thermal conductivity while maintaining the electronic performance. For this strategy to be effective, the nanostructures should be smaller than the phonon mean free path (MFP) but larger than the electron MFP so that phonons are more strongly scattered than electrons. It is understood that both electron and phonon MFPs have a distribution over a certain energy range. There has been good progress in predicting the spectral phonon MFPs for a range of bulk single crystals and alloys [12–24]. However, there has been no discussion on the spectral electron MFPs from first principles. Surprisingly, this status exists even for silicon, one of the most important materials. The existing knowledge on electron scattering, relaxation time, and MFP, is mostly based on analytical models derived from Fermi's golden rule assuming ideal electron and phonon dispersions [25,26]. Past work on the phonon MFP distributions based on first-principles simulations, however, shows that such semi-empirical treatments on scattering lead to large error [13,21,23,27].

In this work, we compute the electron scattering rates and MFPs in silicon from first principles and examine their dependence on energy, doping concentration, and their contributions to electronic conductivity and Seebeck coefficient. We demonstrate quantitatively the large disparity in the electron and phonon MFP distributions in silicon, and use the information obtained to predict that nanostructures with size of 20 nm can result in a higher than five times enhancement in ZT for silicon, consistently with past experimental results.

We consider n-doped silicon with carrier concentration between 10^{16} and $10^{19}\,\mathrm{cm}^{-3}$ in the temperature range

(a)E-mail: gchen2@mit.edu (corresponding author)

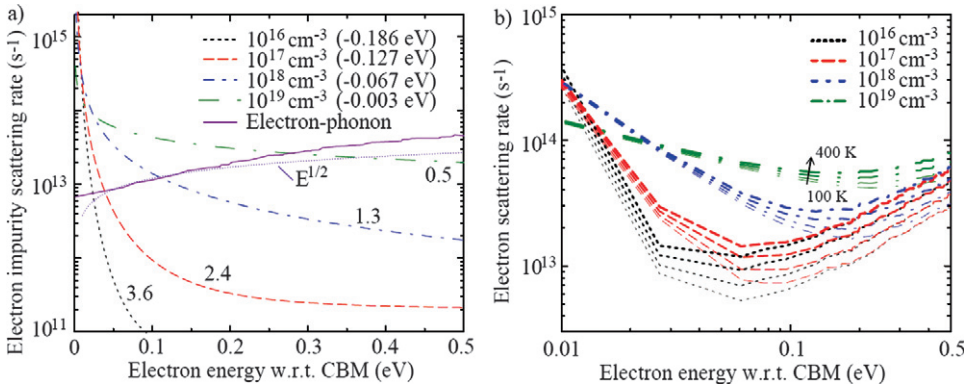

Fig. 1: (Colour on-line) (a) Electron-phonon and electron-impurity scattering rates with carrier concentration between 10^{16} and $10^{19}\,\mathrm{cm}^{-3}$ at 300 K. The chemical potential relative to the band edge is shown inside the parentheses. The numbers near the curves indicate the exponent α in $\tau^{-1} \propto E^{-\alpha}$. (b) The combined electron-phonon and electron-impurity scattering rates.

from 100 to 400 K. In this doping and temperature range, the dominant mechanisms for electron scatterings are electron-phonon and electron-impurity scatterings [28,29]. Both scattering rates are computed under the perturbation framework following Fermi's golden rule. The QUANTUM ESPRESSO package [30] is used to perform all density functional theory (DFT) calculations. In addition, the electron-phonon scattering is computed using the electron-phonon Wannier (EPW) package based on maximally localized Wannier functions [31,32], which allows accurate interpolation of electron-phonon couplings from coarse grids to arbitrarily dense grids [33]. The electron-impurity scattering is computed by explicitly accounting for the long-range Coulomb tail for a screened ionized impurity, which was left out from previous first-principles–based works [28,34]. The Coulomb tail is described using a classical model with inputs from first principles. The inclusion of the long-range Coulomb tail is very important to properly account for the effect of ionized dopants. The details of the computation of electron-phonon and impurity scattering rates, as well as transport coefficients, are summarized in the supplementary information given in [35].

We first show the energy dependence of electron-phonon and electron ionized impurity scattering in fig. 1(a). The Fermi level corresponding to each carrier concentration is given in the corresponding legend. For silicon with n-type doping of $\sim 10^{19}\,\mathrm{cm}^{-3}$, the Fermi level is about right at the conduction band edge at 300 K. Hence, we plotted only results near the band edge. In semiconductors, the electron-phonon scattering is usually assumed to be of the form $E^{1/2}$ for acoustic phonon scattering [29] and fig. 1(a) shows that this approximation starts to break down for an electron energy larger than 0.2 eV and smaller than 0.05 eV. The discrepancy for energies less than 0.05 eV is due to the omission of phonon energy in the energy conservation requirements in deriving the analytical expression [36], which leads to scattering rates that are proportional to the diminishing electron DOS near CBM. With phonon energies explicitly considered in this work, a finite scattering rate results instead. The discrepancy for energy larger than 0.2 eV relates to the deviation from the parabolic band structure. The electron-phonon scattering also differs from analytical predictions for metals, which is of the form $E^{-3/2}$ [37]. The ionized impurity scattering for free-electron scattering from a weakly screened ionized impurity is predicted to be of the form $E^{-3/2}$ while the first-principles results show that the exponent varies from -0.5 to -3.6, in comparison to -1.0 to -1.5 from empirical modeling [26], depending on the carrier concentration. The total electron scattering rate is obtained by summing both scattering channels following Matthiessen's rule $\tau_{\mathrm{el}}^{-1} = \tau_{\text{el-ph}}^{-1} + \tau_{\text{el-imp}}^{-1}$, and is shown in fig. 1(b). The total scattering rate follows the energy dependence of impurity and phonon scattering at low and high energies, respectively. At intermediate energy regimes, the energy dependence shows a continuous transition from impurity to phonon scattering rates. The transition regime shifts to the high energies as impurity density increases. As temperature increases, more phonons are generated and the total scattering rate increases as well.

We compute thermoelectric transport properties based on the Boltzmann transport equation (BTE) and the obtained scattering rate. For example, the electrical conductivity can be expressed as [38]

$$\sigma(T;\mu) = \frac{1}{V}\int \sum_{n\mathbf{k}} w_{\mathbf{k}} \mathrm{e}^2 \Lambda_{n\mathbf{k}} v_{n\mathbf{k}} \delta(\varepsilon - \varepsilon_{n\mathbf{k}}) \times \left[-\frac{\partial f_\mu(T;\varepsilon)}{\partial \varepsilon}\right] \mathrm{d}\varepsilon, \tag{1}$$

where V is the crystal volume, w is the weighting factor, e is the elementary charge, ε is the electron energy, f is the Fermi-Dirac distribution, T is the temperature, and μ is the chemical potential. Λ is the energy-dependent electron MFP obtained by multiplying the electron group velocity v and the energy-dependent relaxation time τ:

$$\Lambda_{n\mathbf{k}}(\varepsilon) = v_{n\mathbf{k}}(\varepsilon) \cdot \tau_{n\mathbf{k}}(\varepsilon). \tag{2}$$

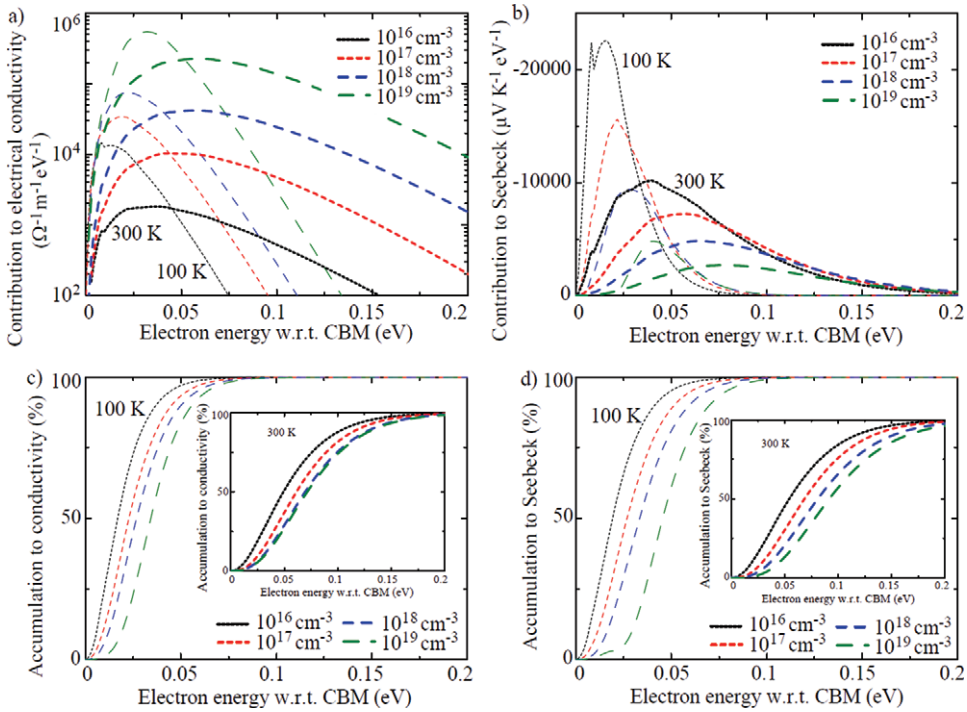

Fig. 2: (Colour on-line) Per-energy interval contribution to electrical conductivity. (b) Per-energy interval contribution to the numerator of the Seebeck coefficient divided by the corresponding electrical conductivity. (c) Percentage accumulation to electrical conductivity. (d) Percentage accumulation to the Seebeck coefficient.

We plot in fig. 2 the dependence of the integrand in eq. (1) for the electrical conductivity (fig. 2(a)) and other thermoelectric properties. At higher temperatures, a wider span of electronic states contributes to transport due to the smearing of the Fermi surface. For the electrical conductivity, the increase in carrier concentration dominates as carrier concentration increases, despite the increased electron scattering rate due to increased electron-impurity scattering. At higher impurity densities, the chemical potential shifts upwards. This leads to lowered average thermal energy for the carriers and, as a result, an overall decrease in the Seebeck coefficient, as seen in fig. 2(b). The double peak in the Seebeck contribution at 100 K near 0.008 eV is due to a numerical error from the band-crossing and it does not affect the results, as seen in fig. 2(d). From fig. 2(c) and (d), it can be seen that the transport is mostly contributed from electronics with energies within 0.2 eV from CBM. The dominant contribution shifts to higher energies as temperature and carrier concentration increase.

The energy-dependent electron MFPs are shown in fig. 3. In general, the electron MFPs depend strongly on both temperature and carrier concentration. The MFPs monotonically decrease with increasing temperatures mainly due to increased electron-phonon scattering rates, which become less important at higher impurity densities. The increase in carrier concentration leads to a monotonic decrease in the MFPs due to the domination of electron-impurity scattering. As seen in fig. 3,

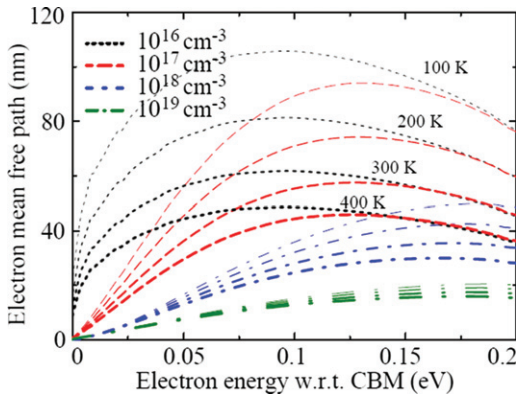

Fig. 3: (Colour on-line) Electron MFP as a function of impurity density and temperature. Thin to thick curves indicate temperatures from 100 to 400 K.

at low temperature and low carrier concentration, the electron MFPs can go up to about 100 nm in silicon at 100 K. The MFPs reduce to about 20 nm with carrier concentration of $10^{19}\,\mathrm{cm}^{-3}$ at 400 K. The MFPs vanish as electron energy approaches CBM. This is because the band structure is parabolic near CBM in silicon so that the band velocity approaches zero as the electron energy approaches CBM, leading to vanishing MFPs. It should also be pointed out that, unlike the distribution of phonon MFP, which spans several orders of magnitude in silicon and tends to diverge at low phonon frequencies [13], the

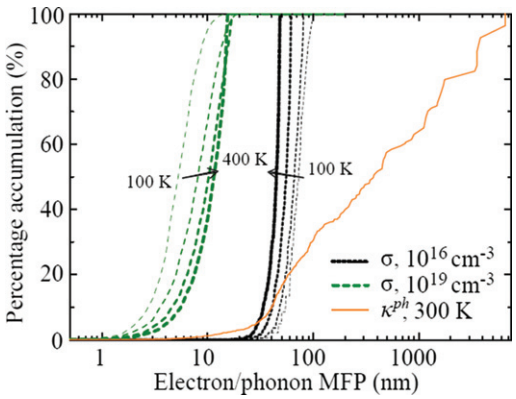

Fig. 4: (Colour on-line) Electrical and lattice thermal conductivity accumulation with respect to MFPs. Thin to thick curves indicate temperatures from 100 to 400 K.

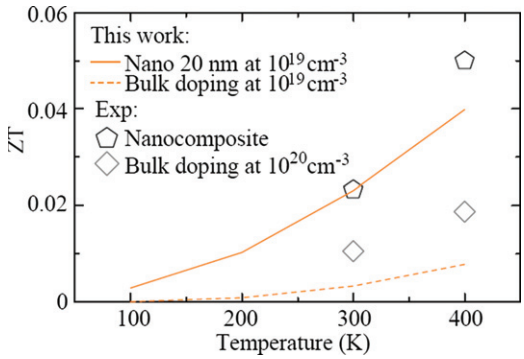

Fig. 5: (Colour on-line) Predicted enhancement in thermoelectric figure of merit ZT due to nanostructuring. Experiments are from ref. [41].

electron MFP in silicon shows much narrower span and does not diverge throughout the energy range relevant to the electron transport.

To understand how energy carriers are affected by nanostructuring, it is useful to make an accumulation plot of electrical/thermal conductivity with respect to electron/phonon MFPs. The accumulation of phonon thermal conductivity with MFP has been extensively studied and has been documented elsewhere [13,39]. The contribution to electrical conductivity from electrons with MFPs up to Λ can be obtained according to eq. (1) by summing over contributions from all electrons with MFPs less than that of Λ:

$$\sigma(\Lambda) = \frac{\mathrm{e}^2}{N_{\mathbf{k}} V} \sum_{n\mathbf{k}}^{\Lambda_{n\mathbf{k}}<\Lambda} \left[-\frac{\partial f_\mu(T;\varepsilon)}{\partial \varepsilon} \right]_{\varepsilon_{n\mathbf{k}}} v_{n\mathbf{k}} \Lambda_{n\mathbf{k}}. \quad (3)$$

Here $N_{\mathbf{k}}$ is the number of k-points. The electron MFP contribution is weighted strongly by the derivative of the Fermi-Dirac distribution. As a result, only electrons with energy falling into the Fermi window contribute mostly to the electrical conductivity.

The accumulation plots for both electrons and phonons in silicon are compared in fig. 4. The electron MFPs show much narrower span in comparison to phonon MFPs. At $10^{19}\,\mathrm{cm}^{-3}$ doping, the majority of the electrical conductivity contributions comes from electrons with MFPs less than 10 nm. The trends of the temperature dependence of the MFPs are opposite for carrier concentrations of 10^{16} and $10^{19}\,\mathrm{cm}^{-3}$. At $10^{16}\,\mathrm{cm}^{-3}$, the MFP shortens at elevated temperatures due to the increased scattering. At $10^{19}\,\mathrm{cm}^{-3}$, the main contribution to electrical conductivity shifts to longer MFP at higher temperatures. This is due to the broadened Fermi window that includes more contributions from electrons with longer MFPs. Note that the phonon accumulation shown here only includes phonon-phonon scattering effects while electron-phonon [40] and phonon-impurity [20] scatterings are not considered in this work. The inclusion of electron-phonon scattering can lead to a ∼7% reduction in the overall lattice thermal conductivity at an electron concentration of $10^{19}\,\mathrm{cm}^{-3}$ [40].

Good thermoelectric materials require low thermal conductivity and good electrical conductivity. According to fig. 4, nanostructures with size of about 20 nm can be chosen to maximally scatter phonons while retaining most of the electron transport at carrier concentrations of $10^{19}\,\mathrm{cm}^{-3}$. To evaluate the effect of nanostructuring in Si, we re-compute the thermoelectric transport coefficients by adding the boundary scattering rates ($\tau_{\mathrm{b}}^{-1} = v/D$) to the bulk scattering rates following Matthiessen's rule for both electrons and phonons. In fig. 5, we show the simulated thermoelectric figure of merit for both bulk Si and nanocrystalline Si, and compare it with the available experimental data. For nanocrystalline Si, we take $d = 20$ nm to be close to the experimentally reported average grain size. The figure shows that simulation results are in reasonable agreement with experiments for both bulk Si crystals and bulk nanocomposites [41]. The predicted ZT of the nanostructured bulk Si is five times higher than that of bulk single crystals. We point out that experimental data are available for carrier concentration at $10^{20}\,\mathrm{cm}^{-3}$ and our simulation can only reach $10^{19}\,\mathrm{cm}^{-3}$ [35]. At the carrier concentration of $10^{20}\,\mathrm{cm}^{-3}$, less electrical conductivity reduction can be expected due to shorter bulk electron MFP and weaker boundary scattering, which may translate into higher ZT.

In summary, we have computed electron scatterings and MFPs in silicon from first principles, and found that the energy dependence of ionized impurity scattering rate differs significantly from the existing analytical expressions. Our simulations show large disparity of electron and phonon MFPs distributions that favor nanoengineering in silicon to improve the thermoelectric figure of merit ZT. We predicted that nanostructures with size of 20 nm can result in a higher than five times enhancement in ZT for silicon doped at $10^{19}\,\mathrm{cm}^{-3}$, owing to the strong scattering of phonons and less-affected electron transport, and the results are in reasonable agreement with the past

experiment. Our work shows the potential of using first-principles tools in engineering nanostructures for thermoelectric energy conversion.

* * *

We would like to thank Dr David Singh, Dr Feliciano Giustino and Dr Vincenzo Lordi for insightful discussions. This work was supported as part of the Solid-State Solar-Thermal Energy Conversion Center (S3TEC), an Energy Frontier Research Center funded by the US Department of Energy, Office of Science, Office of Basic Energy Sciences (Grant No. DE-SC0001299). ODR acknowledges support from the Center for Emergent Materials at The Ohio State University, an NSF MRSEC (Grant No. DMR-0820414).

REFERENCES

[1] Hicks L. and Dresselhaus M., *Phys. Rev. B*, **47** (1993) 12727.
[2] Hsu K. F., Loo S., Guo F., Chen W., Dyck J. S., Uher C., Hogan T., Polychroniadis E. K. and Kanatzidis M. G., *Science*, **303** (2004) 818.
[3] Snyder G. J. and Toberer E. S., *Nat. Mater.*, **7** (2008) 105.
[4] Poudel B., Hao Q., Ma Y., Lan Y., Minnich A., Yu B., Yan X., Wang D., Muto A., Vashaee D., Chen X., Liu J., Dresselhaus M. S., Chen G. and Ren Z., *Science*, **320** (2008) 634.
[5] Biswas K., He J., Blum I. D., Wu C.-I., Hogan T. P., Seidman D. N., Dravid V. P. and Kanatzidis M. G., *Nature*, **489** (2012) 414.
[6] Luckyanova M. N., Garg J., Esfarjani K., Jandl A., Bulsara M. T., Schmidt A. J., Minnich A. J., Chen S., Dresselhaus M. S., Ren Z., Fitzgerald E. A. and Chen G., *Science*, **338** (2012) 936.
[7] Liao B., Zebarjadi M., Esfarjani K. and Chen G., *Phys. Rev. Lett.*, **109** (2012) 126806.
[8] Zebarjadi M., Liao B., Esfarjani K., Dresselhaus M. and Chen G., *Adv. Mater.*, **25** (2013) 1577.
[9] Tian Z., Lee S. and Chen G., *J. Heat Transfer*, **135** (2013) 061605.
[10] Minnich A. J., Dresselhaus M. S., Ren Z. F. and Chen G., *Energy Environ. Sci.*, **2** (2009) 466.
[11] Zebarjadi M., Esfarjani K., Dresselhaus M. S., Ren Z. F. and Chen G., *Energy Environ. Sci.*, **5** (2012) 5147.
[12] Broido D. A., Malorny M., Birner G., Mingo N. and Stewart D. A., *Appl. Phys. Lett.*, **91** (2007) 231922.
[13] Esfarjani K., Chen G. and Stokes H., *Phys. Rev. B*, **84** (2011) 085204.
[14] Ward A. and Broido D. A., *Phys. Rev. B*, **81** (2010) 085205.
[15] Wang Y., Qiu B., McGaughey A. J. H., Ruan X. and Xu X., *J. Heat Transfer*, **135** (2013) 91102.
[16] Qiu B., Bao H., Zhang G., Wu Y. and Ruan X., *Comput. Mater. Sci.*, **53** (2012) 278.
[17] Ward A., Broido D., Stewart D. and Deinzer G., *Phys. Rev. B*, **80** (2009) 125203.
[18] Luo T., Garg J., Shiomi J., Esfarjani K. and Chen G., *EPL*, **101** (2013) 16001.
[19] Liao B., Lee S., Esfarjani K. and Chen G., *Phys. Rev. B*, **89** (2014) 035108.
[20] Garg J., Bonini N., Kozinsky B. and Marzari N., *Phys. Rev. Lett.*, **106** (2011) 045901.
[21] Tian Z., Garg J., Esfarjani K., Shiga T., Shiomi J. and Chen G., *Phys. Rev. B*, **85** (2012) 184303.
[22] Lee S., Esfarjani K., Mendoza J., Dresselhaus M. S. and Chen G., *Phys. Rev. B*, **89** (2014) 085206.
[23] Shiomi J., Esfarjani K. and Chen G., *Phys. Rev. B*, **84** (2011) 104302.
[24] Lindsay L., Broido D. A. and Reinecke T. L., *Phys. Rev. Lett.*, **111** (2013) 025901.
[25] Pop E., *Annu. Rev. Heat Transfer.*, **8** (2014) 1.
[26] Lundstrom M., *Fundamentals of Carrier Transport*, 2nd edition (Cambridge University Press) 2009, p. 440.
[27] Zebarjadi M., Esfarjani K., Dresselhaus M. S., Ren Z. F. and Chen G., *Energy Environ. Sci.*, **5** (2012) 5147.
[28] Restrepo O. D., Varga K. and Pantelides S. T., *Appl. Phys. Lett.*, **94** (2009) 212103.
[29] Lundstrom M., *Fundamentals of Carrier Transport*, 2nd edition (Cambridge University Press) 2002, p. 230.
[30] Giannozzi P., Baroni S., Bonini N., Calandra M., Car R., Cavazzoni C., Ceresoli D., Chiarotti G. L., Cococcioni M., Dabo I., Dal Corso A., de Gironcoli S., Fabris S., Fratesi G., Gebauer R., Gerstmann U., Gougoussis C., Kokalj A., Lazzeri M., Martin-Samos L., Marzari N., Mauri F., Mazzarello R., Paolini S., Pasquarello A., Paulatto L., Sbraccia C., Scandolo S., Sclauzero G., Seitsonen A. P., Smogunov A., Umari P. and Wentzcovitch R. M., *J. Phys.: Condens. Matter*, **21** (2009) 395502.
[31] Giustino F., Cohen M. and Louie S., *Phys. Rev. B*, **76** (2007) 165108.
[32] Noffsinger J., Giustino F., Malone B. D., Park C.-H., Louie S. G. and Cohen M. L., *Comput. Phys. Commun.*, **181** (2010) 2140.
[33] Park C.-H., Bonini N., Sohier T., Samsonidze G., Kozinsky B., Calandra M., Mauri F. and Marzari N., *Nano Lett.*, **14** (2014) 1113.
[34] Lordi V., Erhart P. and Åberg D., *Phys. Rev. B*, **81** (2010) 235204.
[35] `http://arxiv.org/abs/1409.4862`.
[36] Grimvall G., *The Electron-Phonon Interaction in Metals* (North-Holland Publishing Company, USA, Canada; Elsevier North-Holland) 1981, p. 304.
[37] Wilson A. H., *The Theory of Metals* (Cambridge University Press, Cambridge, UK) 1953.
[38] Scheidemantel T., Ambrosch-Draxl C., Thonhauser T., Badding J. and Sofo J., *Phys. Rev. B*, **68** (2003) 125210.
[39] Tian Z., Esfarjani K., Shiomi J., Henry A. S. and Chen G., *Appl. Phys. Lett.*, **99** (2011) 053122.
[40] Liao B. L., Qiu B., Zhou J. W., Huberman S., Esfarjani K. and Chen G., to be published in *Phys. Rev. Lett.* (2015).
[41] Bux S. K., Blair R. G., Gogna P. K., Lee H., Chen G., Dresselhaus M. S., Kaner R. B. and Fleurial J.-P., *Adv. Funct. Mater.*, **19** (2009) 2445.